Rarefied, superorbital flows in an expansion tube

V. Wheatley, H.S. Chiu, P.A. Jacobs, M.N. Macrossan, D.J. Mee and R.G. Morgan

Department of Mechanical Engineering, Centre for Hypersonics, The University of Queensland, Brisbane, Australia

Abstract *This paper describes a free-piston driven expansion tube and its instrumentation. The facility is used to generate rarefied flows at speeds of approximately 10 km/s. Although the flow in the tube itself is in the continuum regime, rarefied flow conditions are achieved by allowing the test gas to further expand as a free jet into the facility's test section. The test flow is surveyed to provide bar-gauge pressure measurements. Numerical simulation is then used to describe more fully the test flow properties. The flows produced are suitable for the aerodynamic testing of small models at superorbital speeds and should provide data that are suitable for the calibration of Direct Simulation Monte-Carlo codes.*

Introduction

In the past decade, there has been a resurgence of interest in rarefied, hypervelocity flows. This interest can be chiefly attributed to two factors; the increasing use of aerobraking maneuvers to save fuel on interplanetary missions (Moss, 1995), and the fact that a greater understanding of rarefied hypervelocity flows is required to optimise the design of re-entry vehicles (Gupta *et al.*, 1997). In particular, accurate predictions of the surface heating, temperature, and flow field quantities during re-entry are required so that the weight of the thermal protection system can be minimised in order to increase the payload capacity. Obtaining accurate predictions by computational fluid dynamics (CFD) methods requires accurate modelling of the flow field chemistry, gas-surface interaction, body and shock slip and the thermochemical nature of the flow field (Gupta, 1996).

Owing to the extreme conditions encountered during re-entry, and the associated modelling difficulties, it becomes essential to calibrate the CFD codes against the experimental data for a wide range of flow conditions. While some codes have proven to be accurate for the flows that can be obtained in present ground based test facilities, calibration for the high energy, rarefied hypervelocity flows encountered during re-entry has only been possible using relatively scarce flight data. The most suitable numerical technique for the

calculation of the flow properties is the Direct Simulation Monte Carlo (DSMC) method (Bird, 1994), in which the motions and collisions of the gas molecules are simulated on a computer. Gupta *et al.* (1997) compared the results from DSMC and a number of continuum CFD codes with the flight data from the Japanese Orbital Re-entry Experiment (OREX) vehicle. While the flight data agreed quite well with the DSMC predictions for altitudes greater than 84 km, there were still significant discrepancies at altitudes of around 95 km.

To remedy this situation an experimental validation of DSMC for hypervelocity conditions should be undertaken. Unfortunately, present experimental facilities that produce rarefied gas flows (such as the DLR Göttingen continuous operation hypersonic vacuum wind tunnel (Dankert, 1996) and the SR3 low density facility (Allegre, 1992)) are limited to stagnation temperatures of around 2,500 K and hence test speeds of under 2.5 km/s, whereas a flow speed of the order of 10 km/s is required to simulate the conditions encountered during an aerobraking maneuver.

One possible method for generating rarefied hypervelocity flows is to modify an expansion tube (Morgan, 1997). In 1998, a pilot study was conducted on the development of a rarefied hypervelocity test facility using the X1 expansion tube at The University of Queensland (Wendt *et al.*, 1998). In the pilot study rarefied flow was generated by operating the tube at low densities and then expanding the flow into the dump tank via a conical nozzle attached to the exit of the tube. This generated a flow of argon in the transitional regime at 8.8 km/s, with a test flow duration of 60 μs. A 50 mm diameter central core flow was produced with a spanwise Pitot pressure variation of 30 per cent. Unfortunately, these variations make the flow unsuitable for most experiments, where a nominally uniform core flow is required. Another problem identified in the pilot study was the unacceptable large amount of time-variation in the experimental data. In addition to this, there were found to be significant differences between the experimental data and the results from a CFD simulation, pointing to inadequacies in the simulation technique.

To continue the study into developing a rarefied hypervelocity test facility, a new series of experiments has been conducted using a free jet to expand a flow of nitrogen into the dump tank (Macrossan *et al.*, 2000). The results of these experiments consist of Pitot pressure histories at discrete locations throughout the dump tank and static pressure histories at several points along the expansion tube from which shock speeds can be calculated. More information on the flow field is required before precise testing can be carried out in the facility. This information could be obtained from an accurate CFD model of the flow through the facility.

This paper presents the experimental data in conjunction with computational estimates. Once the accuracy of the CFD model has been verified, more detailed information can be extracted from the simulation data that is available from the experimental data. Most importantly, it is possible to

quantify the variation of flow parameters across the test flow; this determines whether or not the flow is suitable for experiments. The divergence of the core flow can also be determined along with the degree of rarefaction of the flow. The final CFD model can also be used to predict the performance of the experimental facility at different operating conditions. This enables the establishment of a tentative range of rarefied flows that can be produced in the facility.

Experimental facility

The X1 expansion tube at the University of Queensland is a small scale, free piston-driven expansion tube (Paull *et al.*, 1988). X1 was the first expansion tube to be driven by a free piston driver and could be used to produce superorbital flows (i.e. flight speed above 8 km/s or total enthalpy over 30 MJ/kg), with test speeds of up to 13 km/s.

The layout of X1 configured with a simple free-piston driver is shown in Figure 1. The facility consists of the following components: a high pressure cylinder called the compression tube, which initially contains the driver gas and the 3.4 kg free piston; an annular reservoir which stores the compressed air that is used to drive the free piston; a lower pressure cylinder referred to as the shock tube, which initially contains the test gas; a cylinder referred to as the acceleration tube, which is initially filled with very low pressure acceleration gas; and finally, a large dump tank/test section with a volume of $0.15\,\mathrm{m}^3$ which is also initially filled with low pressure acceleration gas. The geometries of sections were: compression tube length of 2.30 m and internal diameter of 100 mm; shock tube length of 2.09 m and diameter of 38.1 mm; acceleration tube length of 2.91 m and diameter of 38.1 mm.

The driver and shock tube are separated by a steel diaphragm known as the primary diaphragm. During operation of the facility, the compressed air in the annular reservoir propels the free piston down the compression tube, compressing the driver gas. At some point, the pressure of the driver gas exceeds the burst pressure of the primary diaphragm, causing it to rupture. The high pressure driver gas then expands into the shock tube and generates a shock wave that rapidly compresses the low pressure test gas. This shock wave, which is referred to as the primary shock, propagates along the length of
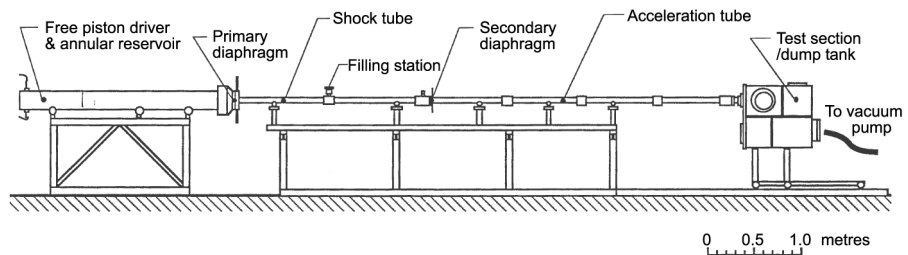

Figure 1.
Layout of the X1 expansion tube

the shock tube compressing and accelerating the test gas. This process is illustrated via the distance-time (x-t) wave diagram in Figure 2, along with the other processes that occur in X1.

Upon reaching the end of the shock tube, the primary shock ruptures the light plastic secondary diaphragm, which initially separates the test gas from the acceleration gas. For ideal expansion tube operation, the secondary diaphragm is assumed to be massless and to rupture instantaneously, (Figure 2). The compressed test gas is then processed by an unsteady expansion and begins to expand into the acceleration tube generating the secondary shock, which compresses and accelerates the low pressure acceleration gas. The unsteady expansion that propagates upstream through the test gas (downstream in the laboratory reference frame as expansion waves travel at velocity u-a and the shock compressed test gas is supersonic) serves to expand it to the desired test conditions. The test flow begins with the passage of the contact surface between the acceleration and the test gas past the model location. The test flow at the model location is terminated by one of the following two events; the arrival of the tail of the unsteady expansion, or the arrival of the disturbance caused by the reflection of the head of the expansion off the contact surface between the driver and the test gas.

Usually, the expansion tube facilities are operated in such a way as to produce flows with high static and total pressures. To generate a rarefied hypervelocity test flow in X1, relatively low initial fill pressures were used in the shock and acceleration tubes. The resultant flow at the end of the acceleration tube was then further expanded as a free jet into the dump tank. Helium was used as the driver gas and nitrogen was used as both test and acceleration gases. The set of nominal fill conditions used in the experiments include 536 Torr of helium in the compression tube, 14.5 Torr nitrogen in the shock tube and 15 Pa nitrogen in the acceleration tube and dump tank. It is assumed that the gas temperatures, after filling, were same as the ambient temperature of 296 K. The primary steel diaphragm had a thickness of 0.55 mm and a burst pressure of approximately 19.3 MPa. The light, secondary diaphragm consisted of 23 μm thickness cellophane with an approximate burst pressure of 100 kPa.
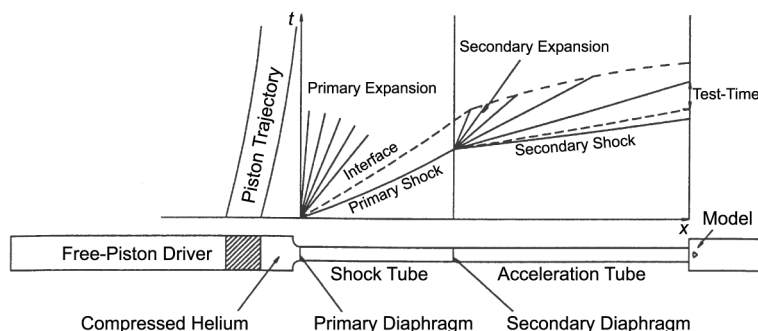

Figure 2.
Ideal wave diagram of the shock and expansion processes that produce the test flow in X1

Instrumentation
The flow field in the dump tank was surveyed using bar gauges specifically designed to give fast response Pitot pressure measurements in the impulsively started flow. Surveys of the radial Pitot pressure distribution were made at six axial locations between 25 and 340 mm from the exit of the acceleration tube. Bar gauges were used in preference to conventional Pitot probes with piezoelectric pressure transducers due to slow response of such probes in low-density, short duration flows. This poor performance was due to the shielding that was used to protect the pressure transducer from erosion caused by diaphragm fragments travelling at high speeds with the flow. The bar gauges used during low density operation of X1 are shown in Figure 3. They are a modified form of the conventional bar gauge. To improve the aerodynamic shielding of the bar and the survivability of the gauge, a steel disc of 9 mm diameter and 1 mm thickness was attached to the front of each bar. Although the addition of the disc slows the response of the bar gauge, its rise time is still only around 5 μs.

Two types of strain sensing elements were used in the bar gauges during the program of low-density testing in X1: piezoelectric polymer films (Smith and Mee, 1996) and semiconductor strain gauges (Kulite type ACP-120-300). Piezoelectric film with an axial length of 10 mm was wrapped around each bar, with its most sensitive axis aligned with the bar axis. Two strain gauges were mounted on opposite sides of each bar in a bending compensation arrangement allowing the axial strain in the bar to be measured. The strain gauge amplifier had a rise time of 1 μs.

The calibration of the bar gauges using PCB impact hammers (type 086-C04 and 086-D80) is described by Macrossan *et al.* (2000). The accuracy of this calibration was estimated to be ± 5 per cent. The calibration of the bar gauges was then checked by placing it in a known flow produced by a shock tube. This was done to account for the curved bow shock that forms in front of the gauge, causing the pressure on the disc to vary from close to the Pitot pressure at the center, to lower values near the edge of the disc. From the shock tube tests, the overall uncertainty in the measured disc average pressure was estimated to be ± 7 per cent for average pressures of the same order as those at the exit of the expansion tube. Away from the exit of the tube in the expansion tube tests, the Pitot pressure drops to as low as 3 per cent of the value at the acceleration tube exit causing the uncertainty in the bar gauge measurements to increase. At the most, distant locations included in the flow field survey, the uncertainty

Figure 3.
Bar gauge design for low-density, impulsively started flows
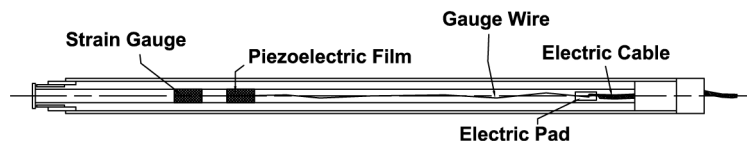
in the disc average pressure was estimated to increase to a maximum of ± 15 per cent.

During the low-density experiments in X1, a large spike in the signal from the strain sensing devices was recorded upon arrival of the flow at the bar gauge locations. The spike duration was typically around $10\,\mu s$ and was attributed to ionization of the flow as it is stagnated at the front of the bar gauge. The spike was separated from the pressure signal by positioning the strain sensing devices on the bar such that the spike had subsided by the time the stress waves generated by the flow arrived at the transducer locations.

Static wall pressure was monitored at a number of locations along the expansion tube using commercially available PCB piezoelectric transducers (111, 112 and 113 series). These transducers have a diameter of 5.5 mm and a response time of between 1 and $2\,\mu s$. The transducers were mounted flush to the tube wall to minimise the response time. The manufacturer's calibration factors were used to convert the recorded voltages to pressures. The designations, locations (distances from the acceleration tube exit), sensitivities, types and serial numbers of the active static pressure transducers in X1s shock tube and acceleration tube are presented in Table I. The static pressure traces from these transducers are used to calculate the primary and secondary shock speeds.

Experimental data

For each test, the static pressures along the tube were recorded at the transducer locations (Table I) and bar gauge pressures were recorded at up to three discrete locations in the dump tank. The data acquired during shot S5_157 are presented here as an example of the data obtained during a typical test. Chiu (2000) gives the report for the full set of experimental data. The static pressure histories measured during this shot by the transducers in the shock tube are shown in Figure 4. Note that the signal from transducer ST2 becomes saturated before any steady level is reached and the recorded traces terminate at the transducer locations before the arrival of the unsteady expansion. The primary shock speed was calculated to be 5.24 km/s from the shock arrival times at the transducer locations. Using this shock speed and assuming

Transducer	Location (mm)	Sensitivity (V/kPa)	Serial number	Transducer type
ST1	3,585	1.508×10^{-4}	8487	111A22
ST2	3,410	1.670×10^{-2}	15290	112A22
ST3	3,233	1.460×10^{-4}	9533	111A22
AT1	2,718	7.304×10^{-3}	14534	112A21
AT3	2,018	1.500×10^{-2}	15292	112A22
AT5	1,076	7.562×10^{-3}	14536	112A21
AT7	376	4.120×10^{-3}	9569	113A21
AT8	120	1.624×10^{-2}	10633	112A22

Table I.
Active static pressure transducers in the shock and acceleration tubes. Distances are measured upstream of the acceleration tube exit
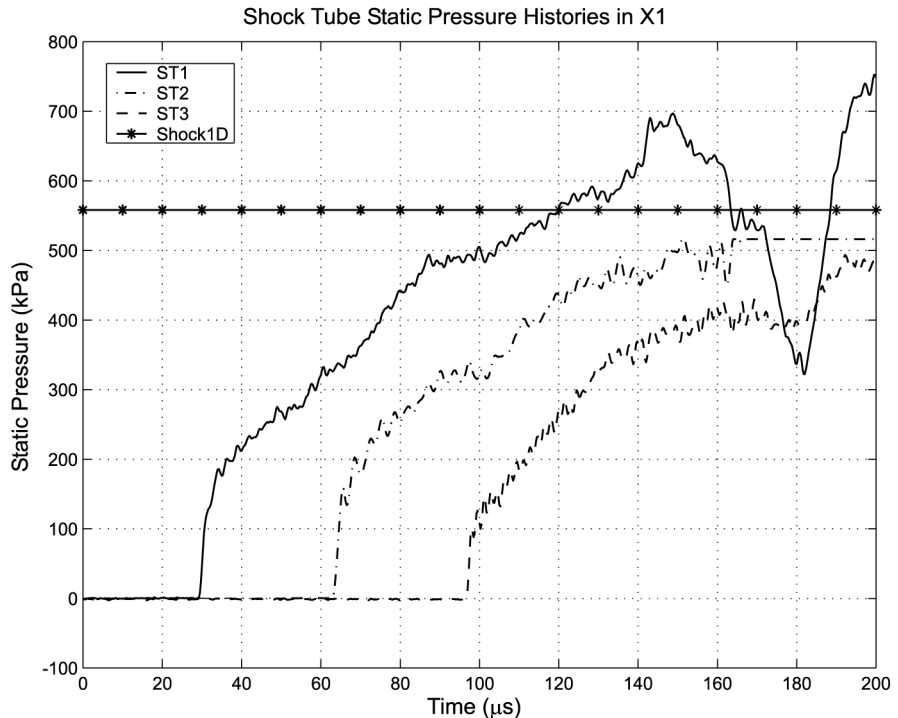
Figure 4.
Measured static pressure
traces from transducers
in the shock tube during
shot S5_157

a one-dimensional shock processing of the test gas (Shock1D), the flow conditions following the passage of the primary shock wave were estimated as: static pressure of 558 kPa, temperature of 7,040 K and a flow speed of 4.79 km/s.

The measured static pressures upstream of the secondary diaphragm show an initial jump with the arrival of the primary shock followed by a gradual rise until reaching the calculated value, approximately 100 μs, after the passage of the shock (Figure 4). Three factors that may contribute to the slow pressure rise behind the primary shock are: non-ideal rupture of the primary diaphragm; piston dynamics; and the geometry of the compression tube. The duration of the pressure rise, approximately 100 μs, is of the same order as the opening time of the diaphragm and it is expected that pressure waves will be generated as the diaphragm opens (Petrie-Repar and Jacobs, 1998). Upon the rupture of the primary diaphragm, an unsteady expansion travels back into the driver gas and, when the expansion propagates into the larger diameter section of the compression tube, compression waves form which travel downstream, gradually raising the pressure in the shock tube above the level behind the primary shock. Assuming quasi-steady flows and given fixed driver gas conditions, the area change in the driver tube may cause a factor of three difference in the driven gas pressure when compared to a constant-area driver. This geometric effect was further explored by Wheatley (2000). The driver and

shock tube transition was modelled with a quasi-one-dimensional CFD code, L1D (Jacobs, 1999). When the unsteady expansion traversed the area change in the driver section, a pressure increase was produced behind the primary shock as expected, however, the pressure rise was small compared with that across the primary shock. Although it was a good candidate, the area change in the driver did not appear to be the cause of the gradual pressure rise observed in the experimental data. The simulations also indicated that the piston dynamics was not the cause either. This issue remains unresolved.

The static pressure histories from four of the transducers in the acceleration tube are shown in Figure 5. It can be seen that, prior to the arrival of the shock, the pressure indicated by the transducers is non-zero in some cases and shows some drift. This is associated with the acceleration sensitivity of the pressure transducers. The effects of transducer drift are most obvious in the low pressure traces near the exit of the acceleration tube. The transducers indicate pressures near the lower limit of their range in these traces. For example, transducer AT7 indicates about 10 kPa but the PCB type 113A21 pressure transducer has a calibrated range of 0.345-1,330 kPa. The reason the gauges are operated near the low end of their range is that they need to be able to
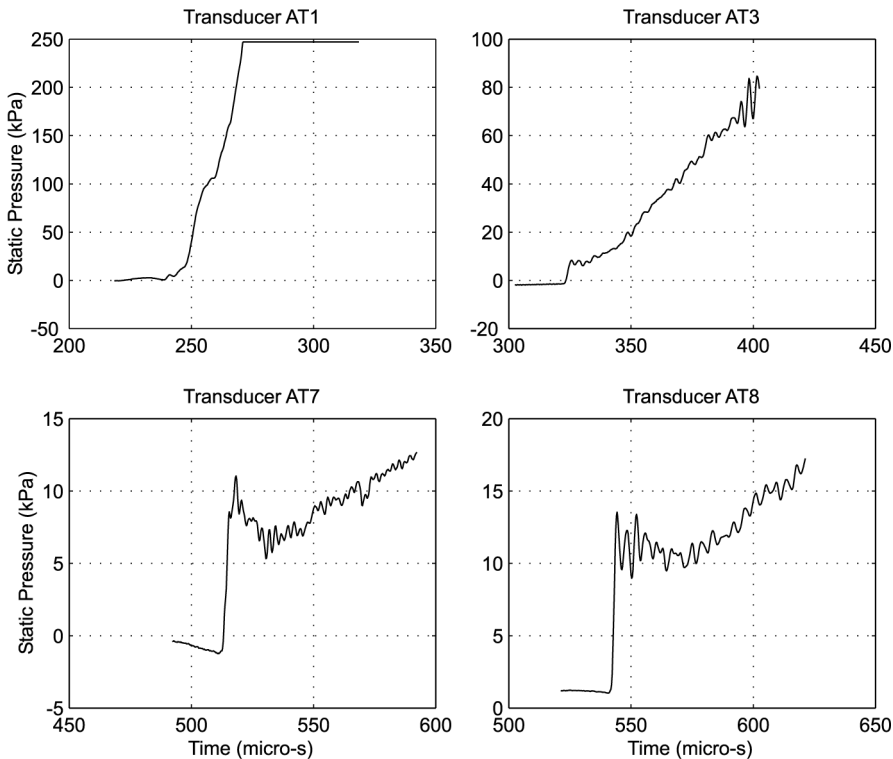

Figure 5.
Measured static pressure
traces from transducers
in the acceleration tube
during shot S5_157

withstand the very high pressure associated with the arrival of the unsteady expansion and, a little later, the arrival of the driver gas. The acceleration effects can be minimised by carefully mounting the transducers in the tube. This was done in the present experiments and the drifts shown in Figure 5 are the smallest that could be achieved with the current transducers. The speed of the secondary shock near the exit of the acceleration tube was estimated to be 8.98 km/s, from the difference between the shock arrival times at transducers AT7 and AT8. The estimated uncertainty in the measured shock speeds is ± 1 per cent. During shot S5_157, three bar gauge pressure histories were recorded at an axial distance of 125 mm from the acceleration tube exit (Figure 6). The histories were recorded on the centerline and at a radius of 28 mm, both above and below the centerline. The noise caused by the ionization of the flow when it first impacts on the bar gauges can be seen in the histories shown in Figure 6 at a time of around 350 μs. To account for shot-to-shot variations from the nominal conditions, the bar gauge pressure histories were normalised by an estimate of the test gas Pitot pressure at the exit of the acceleration tube, $P_{pitot,e}$, for each particular shot. Estimates of the test gas Pitot pressure at the exit plane of the acceleration tube were calculated using the TUBE program (R.G. Morgan, personal communication). TUBE computes the state of the test flow from the fill conditions and experimentally measured shock speeds
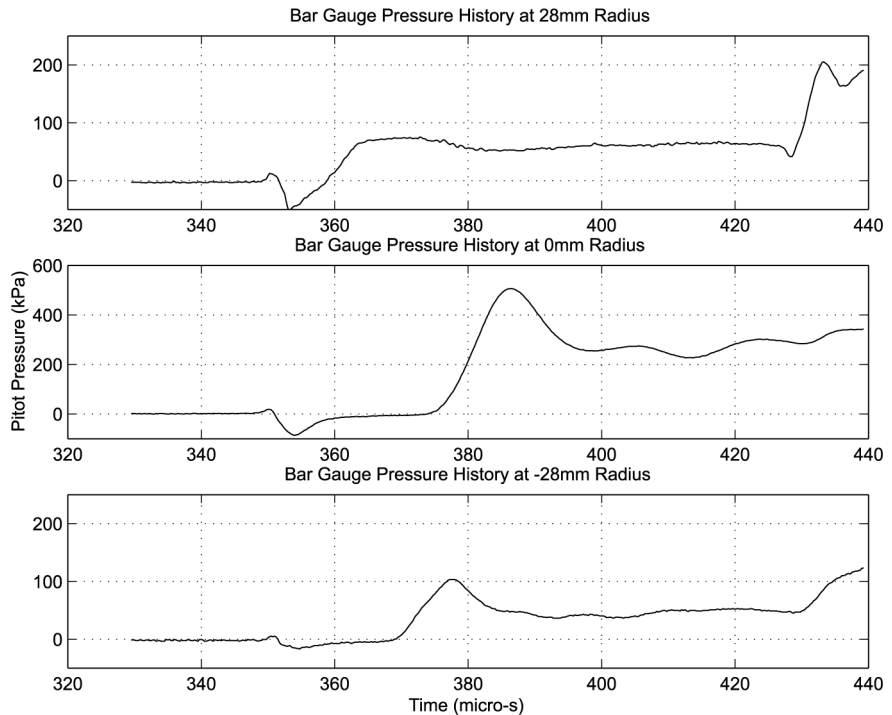

Figure 6.
Measured bar gauge pressure histories from shot S5_157 at 125 mm from the acceleration tube exit

assuming inviscid, one-dimensional flow which is either chemically frozen or in equilibrium. The nominal value of the Pitot pressure at the acceleration tube exit was computed to be 627 kPa. This value was used to normalise the CFD results. The uncertainty in the calculated Pitot pressure is dominated by the ± 1 per cent uncertainty in the secondary shock speed and was estimated to be ± 10 per cent.

The results of the flow field survey at all six axial locations and nine different radii are plotted (Figure 7). The values, $(P_{bar}/P_{pitot,e})_{av}$, are the nominally steady bar gauge pressures of the test gas, which have been normalised by the estimated Pitot pressure at the acceleration tube exit and averaged over a number of tests. For the region within 175 mm of the tube exit plane, the Pitot pressure profile is non-uniform, with a large peak near the centerline. By 225 mm, the Pitot pressure is uniform within experimental uncertainty. Even at this distance, the strong axial gradient of Pitot pressure near the centerline limits the suitability of the flow to the testing of blunt-body models with small axial lengths. From the Pitot pressure histories, it was determined that a nominally steady test time of 50 μs is available at 225 mm from the acceleration tube exit.

It was mentioned previously that the pressure measured using the bar gauges differs from the Pitot pressure due to the pressure variation over the
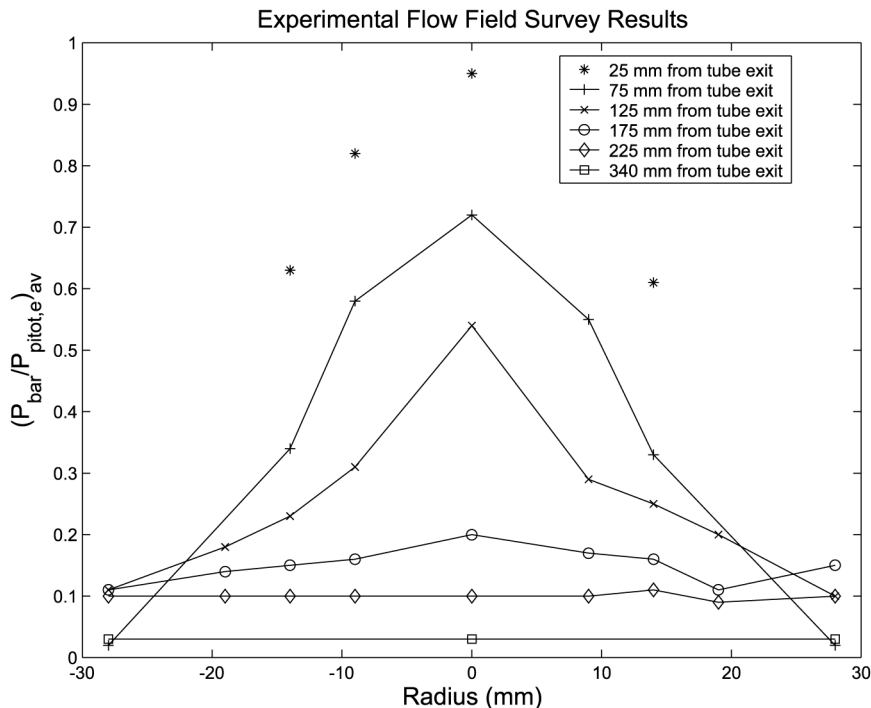

Figure 7.
Experimentally
determined profiles of
normalised, average bar
gauge pressure at several
axial locations in the
dump tank

face of the disc attached to the front of the bar gauge. CFD simulations of nitrogen, impacting on a disc, normal to the flow, were run to determine the pressure distribution on the face of the disc. Both continuum and rarefied gas dynamics codes (Borque, 1999) were used. From these simulations, it was determined that the ratio of the average pressure on the disc to the Pitot pressure varies from around 0.9 or less for continuum flow, to around 0.95, depending on the Knudsen number. As an average adjustment, Pitot pressures computed using the continuum CFD code are multiplied by a factor of 0.93 for comparison with the bar gauge pressures.

Simulation of the acceleration tube flow

The MB_CNS code (Jacobs, 1998) was used to model the hypervelocity flow through the X1 facility. MB_CNS was built to simulate high-enthalpy transient-flow facilities and performs a time-integration of the Navier-Stokes equations for two-dimensional (planar or axisymmetric) compressible flows on a multiple-block structured mesh. The integral form of the governing equations is used, with the flow field being recorded as cell-averaged values. An explicit time-stepping scheme is used to update the conserved quantities within each cell. The code has a shock-capturing capability that is provided by a limited reconstruction of the flow-field data using quadratic patches combined with an adaptive flux calculator that is suitable for flows with very strong shocks. This flux calculator switches between the equilibrium-flux method (EFM) (Macrossan, 1989) and the AUSMDV flux calculator (Wada and Liou, 1994), with the more dissipative EFM, selected for cell interfaces that are near a shock. The code includes thermochemical models for a variety of gas, including nitrogen in chemical equilibrium.

The high speeds of shock waves in the shock tube of the X1 facility cause the shock-processed test gas to reach very high static temperatures, around 10,000 K in some cases. This results in parts of the flow having high levels of dissociation and possibly some ionisation. The test gas cools again as it is processed by the unsteady expansion in the acceleration tube. To determine the conditions of the test gas at the end of the acceleration tube, an ideal (but very expensive) calculation would include the finite-rate chemistry of the shock-compressed and then expanded test gas. Other possibilities are to use equilibrium chemistry or to assume that the test gas chemistry remains frozen at the state behind the primary shock. Neely and Morgan (1994) found that equilibrium chemistry calculations through the unsteady expansion gave results in reasonable agreement with experiments in X1, while frozen chemistry calculations did not. Equilibrium chemistry modelling has been used for the present simulations.

As a shock travels down the acceleration tube, a boundary layer grows in the flow behind it. As this boundary layer becomes quite thick at the end of the tube, it will have a significant influence on the flow field in the dump tank

during the test time. A boundary layer also grows behind the primary shock as it travels down the shock tube. For the operating condition discussed here, this boundary layer will have little effect on the test flow for two reasons. First, the flow in the shock tube has a much higher density and lower velocity than that in the acceleration tube, resulting in a much thinner boundary layer. Second, when the primary shock arrives at the secondary diaphragm, the gas that comprises the test flow is located immediately behind the primary shock where a boundary layer has just begun to grow. The thicker boundary layers further upstream of the secondary diaphragm should have little influence on the test gas as it is expanded down the acceleration tube. The net result of this is that the cross-stream variation in the test gas as it exits the acceleration tube is chiefly due to two-dimensional effects in the acceleration tube. This implies that only the acceleration tube and dump tank must be modelled two-dimensionally, provided an inflow condition at the secondary diaphragm station can be accurately determined from either experimental data or a one-dimensional flow calculation.

The dump tank is actually a rectangular prism, but has been modelled as a cylinder with a radius equal to the minimum distance from the centerline to one of the dump tank walls (Figure 8). Since the simulation time expires before any waves reflected from the modelled dump tank wall encroach on the test flow, this approximation should not affect the estimate of the test conditions. In the simulations, the length of the acceleration tube was taken to be 2.91 m. For convenience, the co-ordinate x is defined as being the axial distance from the exit of the acceleration tube, and the co-ordinate r as being the radial distance from the axis of the acceleration tube.

Inflow conditions
Since the MB_CNS model of the X1 facility is truncated upstream of the secondary diaphragm, an acceleration tube inflow condition is needed. It is possible to make a purely analytical estimation of the performance of an expansion tube, and hence the acceleration tube inflow condition, based on the facility dimensions, fill states and the expected driver performance. Such an
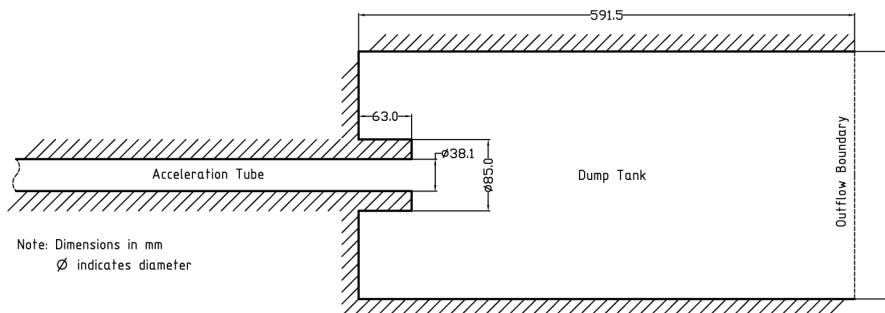

Figure 8.
Modelled geometry of the end of X1's acceleration tube and dump tank. The acceleration tube diameter is 38.1 mm and the dump tank diameter is 295 mm

analysis was carried out by Trimpi (1962) for dissociating air assuming ideal diaphragm rupture. However, experimental investigations have revealed that this approach is inaccurate (Jones, 1965; Shinn and Miller, 1978). Neely (1995) cites viscous effects on the flow, due to the low quiescent gas pressures in the shock and acceleration tubes, as the primary source of the inadequacies of such analytical predictive techniques. He goes on to state that one technique to minimise this complication, and any non-ideal driver effects, is to use the shock speeds observed during the operation of the expansion tube to calculate the shock strengths in the test and acceleration gas. This approach of using experimentally observed shock speeds is adopted to calculate the state of the gas flowing into the acceleration tube, which is initially taken to be the conditions behind the primary shock as it arrives at the secondary diaphragm. Even though the cause of the gradual pressure rise in the shock tube is not known (Figure 4), the flow in the acceleration tube is simulated using a fixed set of post-shock conditions, obtained shortly before the shock arrives at the secondary diaphragm.

Using the conditions behind the primary shock, our inflow conditions assumes that the secondary diaphragm operates ideally. This implies that when the primary shock arrives, the diaphragm material is instantly removed from the flow path so that a reflected shock is not generated. The effects of non-ideal diaphragm rupture were examined by Wheatley (2000) and it was found that the experimental conditions in X1 could be better simulated with the inclusion of a non-ideal diaphragm rupture model. The holding time model used by Wilson (1992) was incorporated into the simulation because the more realistic diaphragm-inertia model (Morgan and Stalker, 1992) could not be easily implemented in a fixed-grid CFD code such as MB_CNS. Equilibrium chemistry modelling was used in preference to a frozen composition as it was shown that this provides a solution in reasonable agreement with that computed using the finite-rate chemistry modelling (Wheatley, 2000).

To implement the holding time model in the MB_CNS simulation, two blocks were added to the computational grid. The first block extends from a location in the shock tube at $x = -3.11$ m to the location of the shock reflected from the secondary diaphragm at the expiration of the holding time. This block initially contains gas with the conditions behind the primary shock.

Roberts *et al.* (1997) calculated effective holding times for a number of light diaphragms used in an expansion tube. This was done by constructing an x-t wave diagram from heat flux signals recorded in the region of the diaphragm, and extrapolating to determine the delay between the impact of the primary shock and the time at which the secondary shock is transmitted into the acceleration tube. For a planar polyethylene diaphragm that is 13 μm (similar to the diaphragms used during low-density testing in X1), the holding time was found to be of the order of 10 μs, over a range of operating conditions. For this

reason, a holding time of $10 \, \mu s$ was adopted and the reflected shock was calculated to be at $x = -2.9185 \, m$, after this the holding time expired.

The second block extends from the reflected shock location to the secondary diaphragm station at $x = -2.91 \, m$, and initially contains gas with the conditions behind the reflected shock. These are a static pressure of 6.83 MPa and temperature of 10,280 K. At these conditions, dissociated nitrogen atoms comprise nearly 42 per cent of the gas mixture and there is a small amount of ionisation.

When this simulation was initiated, there was no barrier to prevent the gas behind the reflected shock from suddenly expanding into the acceleration tube, thus simulating an instantaneous rupture of the secondary diaphragm after the $10 \, \mu s$ holding time.

Grid definition and resolution
The computational models extend from the location $x = -3.11 \, m$ in the downstream end of the shock tube to a plane part way along the dump tank at $x = 0.5285 \, m$. At the inflow plane, the flow condition is the test-gas condition after the passage of the primary shock. The other end of the computational domain is modelled as a supersonic outflow boundary. This assumes that waves do not reflect off the downstream end wall of the dump tank and affect the flow within the simulation time. The computational grid for the acceleration tube has 3,900 cells in the axial direction and 30 cells in the cross-flow direction. The cells are radially clustered towards the wall in order to adequately capture the boundary layer growth. This can be seen in Figure 9, which shows a sample of the computational grid near the exit of the acceleration tube. For the most part, the computational grid for the dump tank has 300 cells in the axial
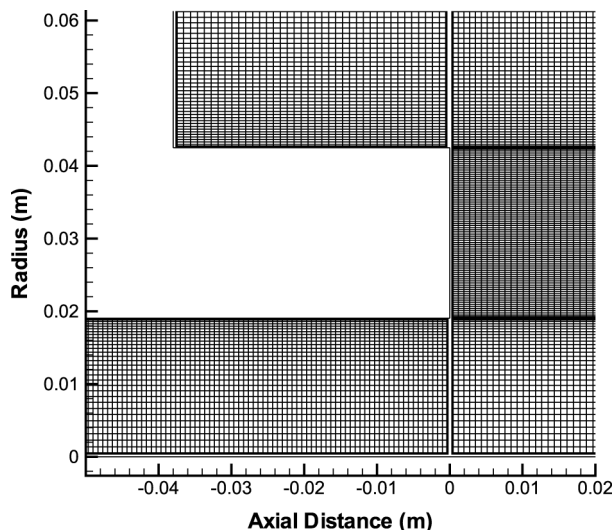

Figure 9.
Sample of the
computational grid at the
entrance of the dump
tank

direction and 210 cells in the cross-flow direction. The cells are initially filled with ambient temperature nitrogen with a pressure of 15 Pa.

This arrangement for the computational grid was arrived after a number of simulations were run on coarser grids, in which some of the flow features did not appear to be adequately resolved. By refining the grid to the current level, the flow features around the shocks and contact surfaces were sharpened, but the overall solution appeared to be grid independent. The final simulation required approximately 100 days of CPU time to solve on an SGI Origin 2000 supercomputer. The physical time taken to run the simulations was considerably less than this, around 30 days, as the simulation was run in parallel on several processors.

Simulation results compared with experimental data

Figure 10 shows a comparison of the computed static pressure histories at four transducer locations along the acceleration tube and the experimental pressure histories from these transducers. The experimental data have been shifted to align the arrival times of the shock. The computed shock speed was found to be 8.1 per cent, greater than the experimental value of 9.06 km/s. This error is significant and may be caused by the use of an equilibrium thermochemical
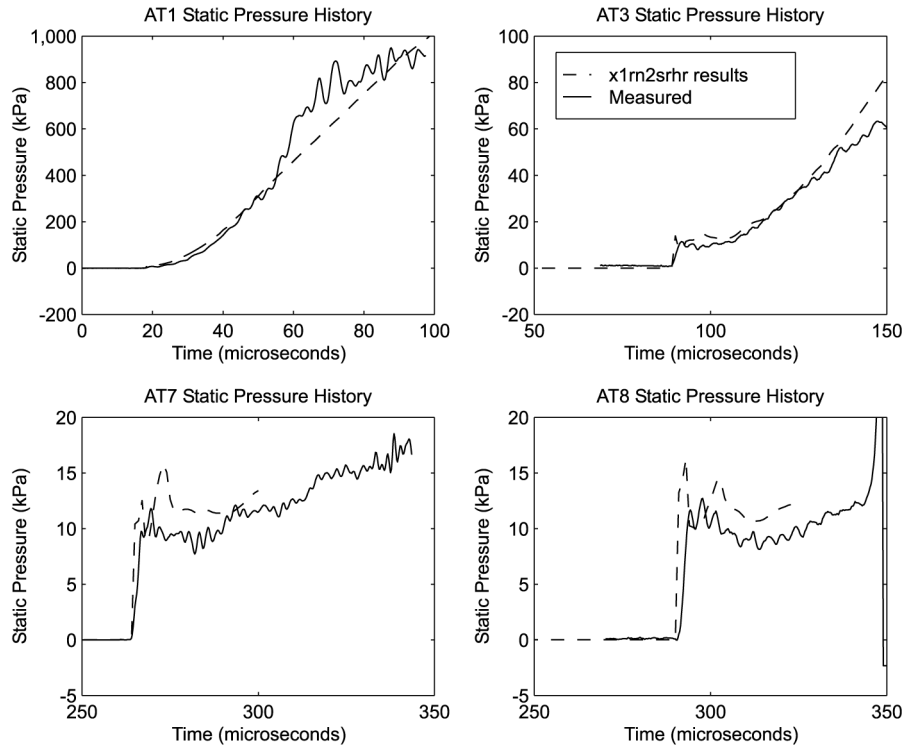

Figure 10.
Aligned computed and experimental static pressure histories in the acceleration tube of X1 at transducer locations AT1 ($x = -2.718$ m), AT3 ($x = -2.018$ m), AT7 ($x = -0.376$ m) and AT8 ($x = -0.120$ m). Experimental values are from shot S7_26

model. A frozen chemistry model produced a significantly lower shock speed so that one can expect a finite-rate chemistry model to perform better.

Despite the difference in shock speed, there is a very good agreement between the shape of the computational and experimental traces at early times (which are relevant to the expanded test flow conditions). The agreement between magnitudes of the computed and experimentally measured pressure histories is also quite good, with the higher pressures behind the shock which is caused by the overestimate of the shock speed. The pressure gradient in the latter part of the simulated expansion may be greater than that which is measured experimentally, because of the unmodelled effects of piston motion and shock tube dynamics. In the results of simulations, without the holding time model (Wheatley, 2000), it was seen that at transducer AT1, the experimental pressure continued to rise after the computed history had leveled off. This problem has been resolved by the inclusion of the holding time model, confirming that a reflected shock is generated during the rupture of the secondary diaphragm.

Figure 11 shows a comparison of the computed and experimental bar gauge pressure histories 175 mm from the exit of the acceleration tube at a radius of 14 mm. It can be seen that the agreement between the nominally steady levels
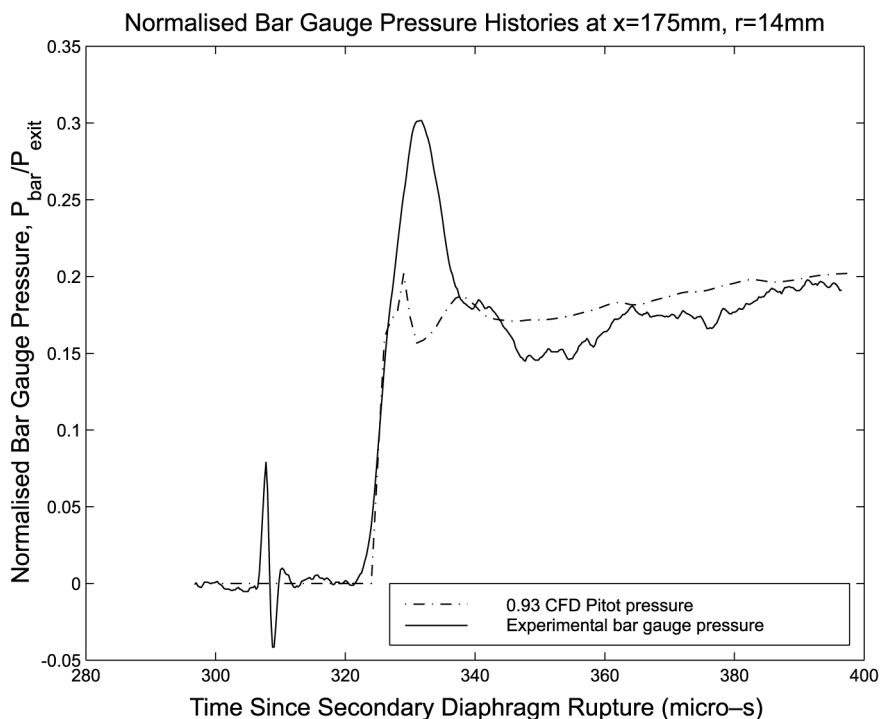

Figure 11.
Normalised bar gauge
pressure histories
175 mm from the exit of
the acceleration tube at a
radius of 14 mm

of the two histories is quite good, however, in this case the magnitude of the Pitot pressure spike due to the reverse shock is far greater in the experimental history.

In Figure 12, a number of Mach number contour plots are presented that show the evolution of the flow field in the dump tank. At the time of the last frame of this figure, $t = 0.34$ ms, the test flow has just arrived at the nominal test location at $x = 225$ mm.

Figures 13-15 show a comparison of the full set of experimental bar gauge pressure profiles in the dump tank and the results of the simulation during the passage of the test gas. The agreement between both the shape and magnitude
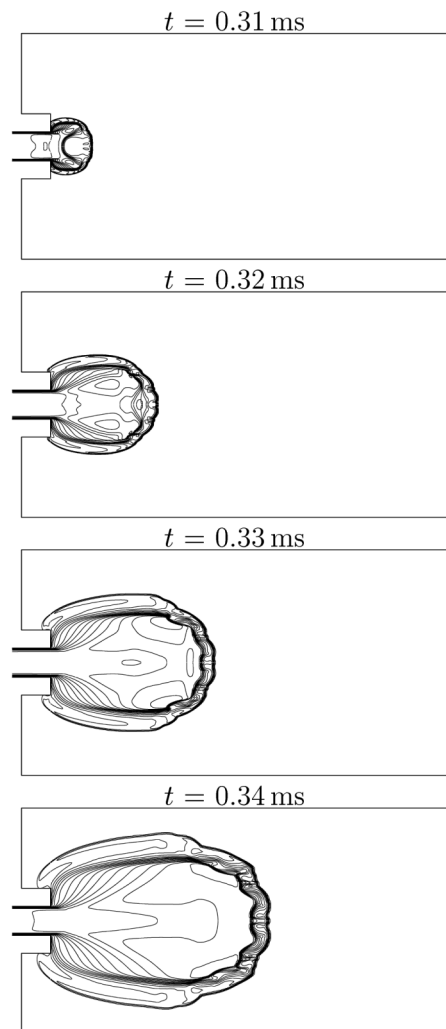

$t = 0.31$ ms

$t = 0.32$ ms

$t = 0.33$ ms

$t = 0.34$ ms

Figure 12.
Contour plots of Mach number showing the evolution of the flow field in the dump tank. Time t is the time since secondary diaphragm rupture
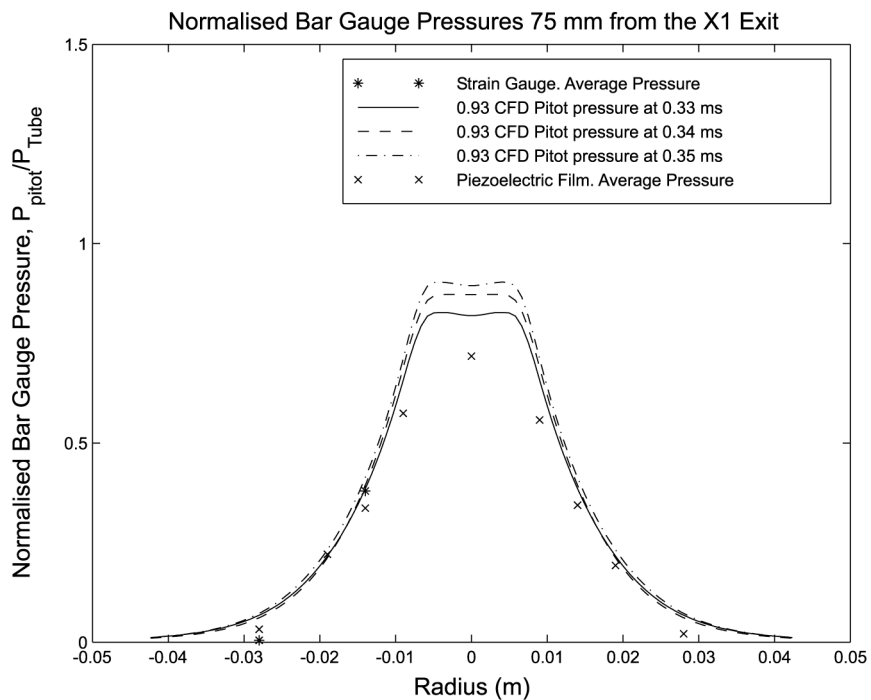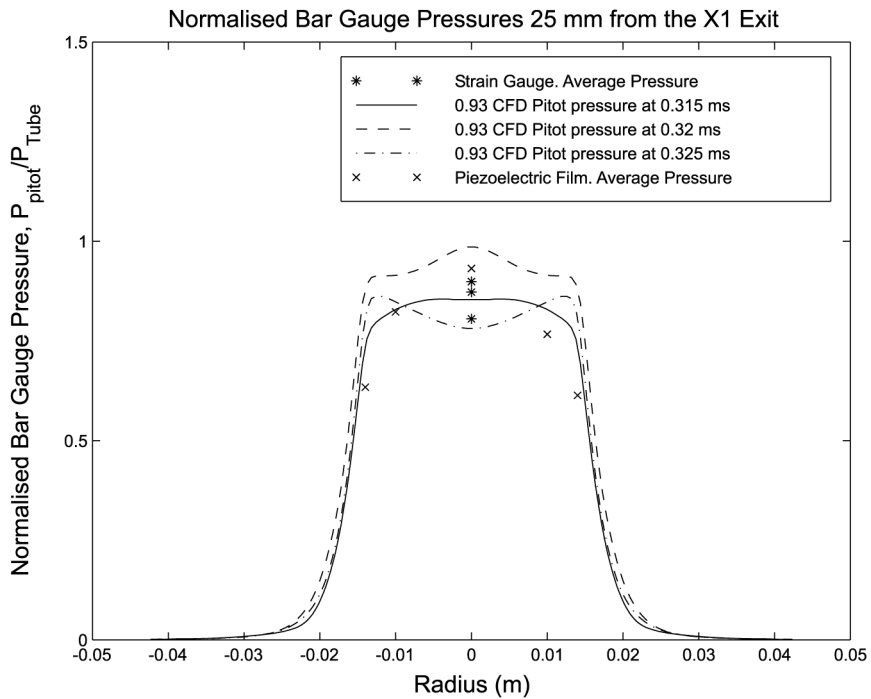
Figure 13.
Normalised bar gauge
pressure profiles in the
X1 dump tank at 25 and
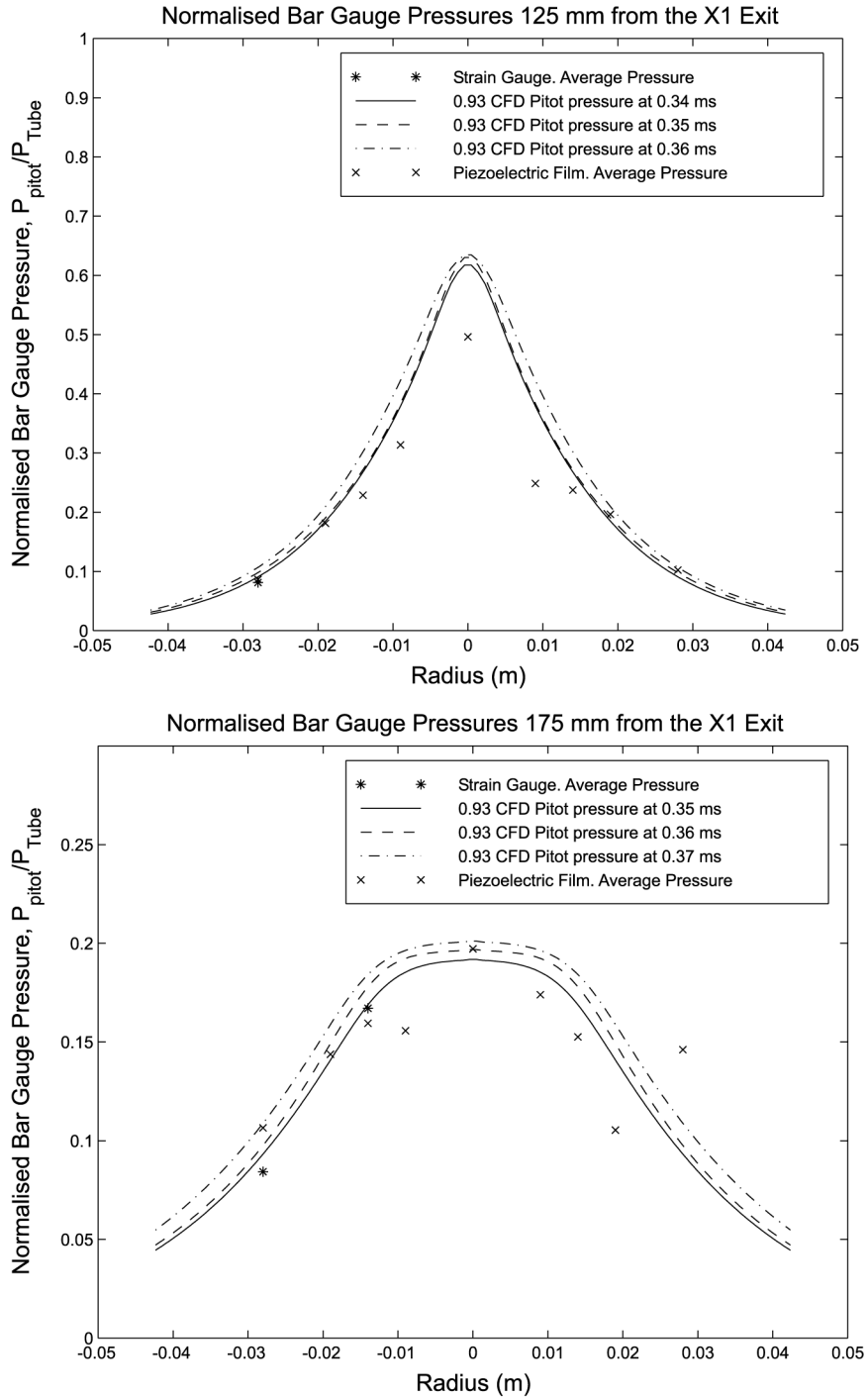75 mm from acceleration
tube exit during the
passage of the test gas

Figure 14.
Normalised bar gauge
pressure profiles in the
X1 dump tank at 125 and
175 mm from
acceleration tube exit
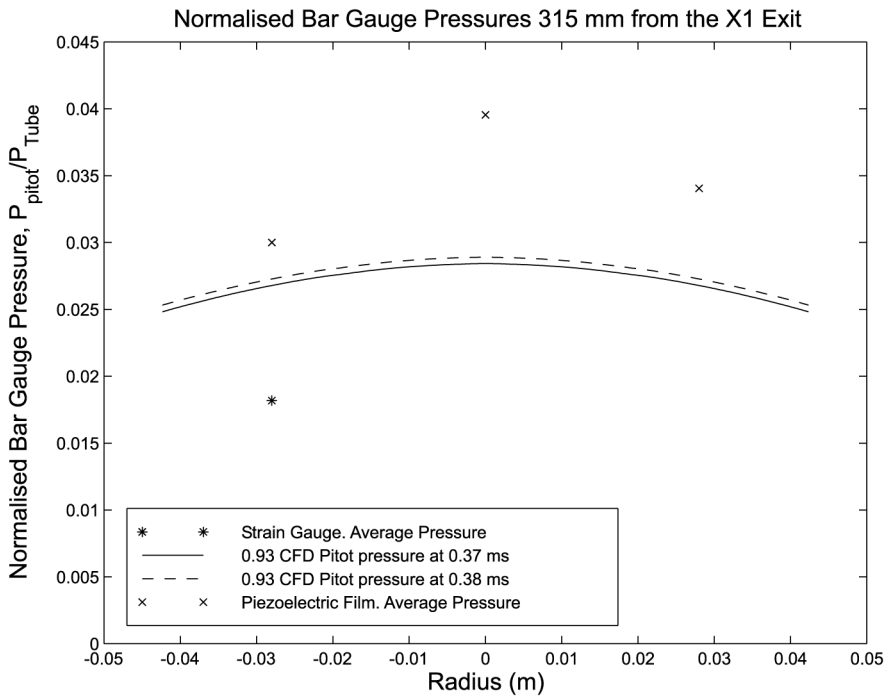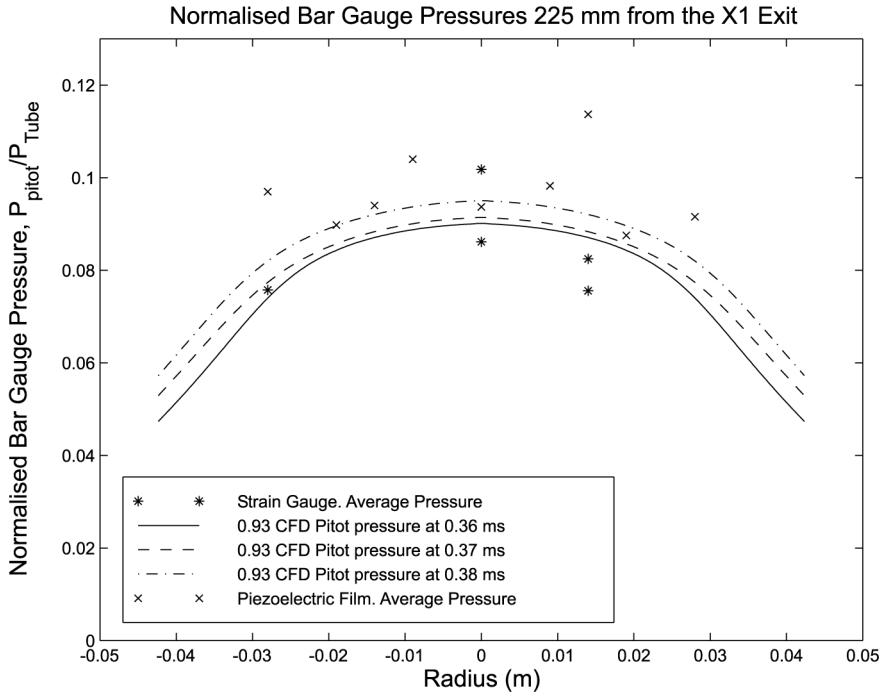during the passage of the
test gas

Figure 15.
Normalised bar gauge
pressure profiles in the
X1 dump tank at 225 and
340 mm from
acceleration tube exit
during the passage of the
test gas

of the computed and experimental profiles is relatively good and, when compared with other simulation results (Wheatley, 2000), confirms that it is important to include the effects of non-ideal secondary diaphragm rupture in a computational model of the facility. From the profiles at 75 and 125 mm from the acceleration tube exit, it can be seen that the computed Pitot pressures near the centerline are slightly overestimated due to the secondary shock speed being overestimated by 8.1 per cent. At $x = 175$ mm, the divergence of the test flow has caused the core of high Pitot pressure flow to be somewhat spread across the dump tank. At the nominal test location, $x = 225$ mm, the Pitot pressure is reasonably uniform near the centerline, indicating that it would be suitable for experiments. The agreement between the computed and experimental profiles is quite good, considering the amount of scatter in the experimental data. In contrast, the experimental values at $x = 340$ mm are considerably higher than the computational results. This may be due to the high degree of rarefaction at axial locations, so far into the dump tank.

Breakdown parameter
For the operating condition used in this study, it was expected that the flow through the majority of facility would be in the continuum regime, only becoming rarefied as it expanded into the dump tank. The validity of using a continuum CFD code (such as MB_CNS) to simulate the low-density flow through X1 is assessed by evaluating the breakdown parameter, P, throughout the facility (Bird, 1994). The breakdown parameter is defined as,

$$P = \frac{\sqrt{\pi}}{2} S \frac{\lambda}{\rho} \left| \frac{\partial \rho}{\partial x} \right|$$

where ρ is the density and S the speed ratio, $u/(2RT)^{0.5}$. Physically, this parameter corresponds to the ratio of the mean time between molecular collisions, τ_c, and the time taken for the flow to traverse a length scale based on the macroscopic gradient of density. In any region of an expanding flow where the breakdown parameter is greater than 0.04, it is probable that the Navier-Stokes equations with no-slip boundary conditions will not give an accurate description of the flow (Bird, 1994). At the instant considered (350 μs), the breakdown parameter only exceeds 0.04 within the free jet into the dump tank. The computed contours of P in this region are shown in Figure 16. It can be seen that the core of the test flow is in the continuum regime, as P is well below 0.04, near the centerline. The high values of P in the flow that has expanded around the corner at the acceleration tube exit indicate that this region of the flow will be subjected to fairly strong non-continuum effects; the characteristic temperatures of the three thermal velocity components will be significantly different. It is expected that the flow in this region will not greatly affect the properties of the test flow near the centerline. The only other regions where the critical
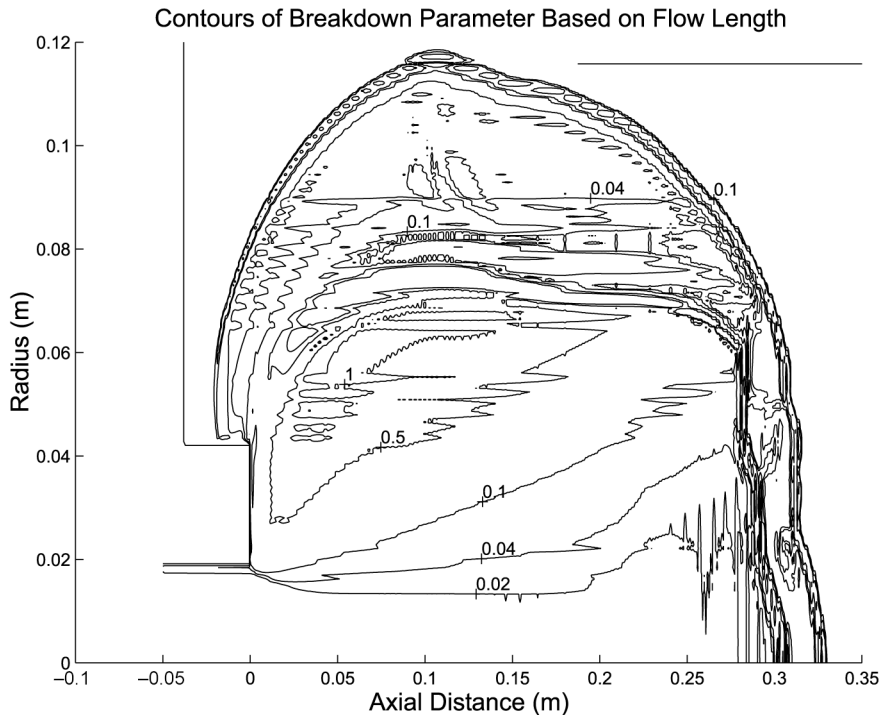
Contours of Breakdown Parameter Based on Flow Length

Figure 16.
Computed contours of
the breakdown
parameter, P, based on
the macroscopic gradient
of density at $t = 350\,\mu s$

value of P is exceeded are within the shocks, however, the accuracy of
shock capturing Navier-Stokes solvers is not significantly affected by the
non-continuum effects that occur within shocks (Cheng and Emanuel, 1995).
Overall, it appears that the accuracy of the estimated core flow conditions
from MB_CNS should not be severely affected by the non-continuum
effects.

One of the goals of this study is to produce a test flow where the breakdown
parameter based on model size, P_D, is of the order of 0.04. The value of P (the
breakdown parameter based on macroscopic flow gradients) being less than
0.04 in the core flow does not compromise this goal because the size of the model
should be considerably less than the length scale based on the macroscopic
flow gradients. This is required to ensure that the flow over the model is
approximately uniform.

Test-section flow properties
The profiles of some important flow properties at the nominal test location,
$x = 225\,mm$, are shown in Figure 17. The profiles shown are from $t = 370\,\mu s$,
at which time the test flow is nominally steady. It is believed that the most
significant errors in the estimated conditions are those in the flow speed, and
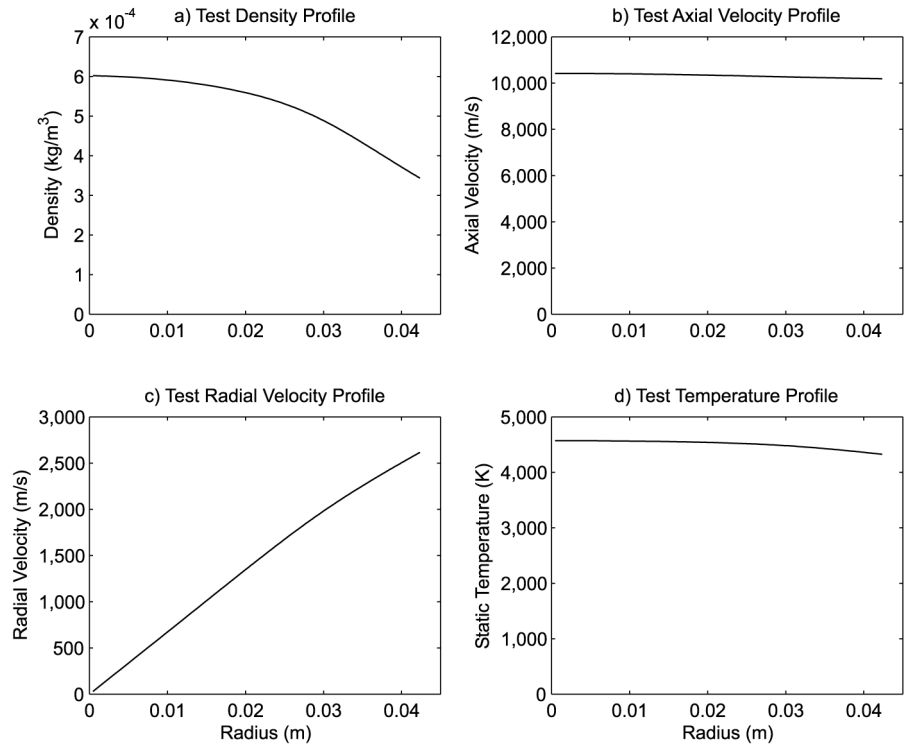hence the Pitot pressure and Mach number. It appears that other quantities

Figure 17.
Computed profiles of
density, axial velocity,
radial velocity and static
temperature at the
nominal test location in
X1, 225 mm from
acceleration tube exit.
Profiles are from
$t = 370\,\mu$s

have been estimated more accurately for the following reasons: the error of
around 17 per cent in Pitot pressure near the centerline at $x = 75\,$mm is
approximately what is expected for an 8 per cent error in flow speed, which
indicates that the estimate of density must be fairly accurate; the static
pressure traces from near the exit of the acceleration tube indicated that the
static pressure of the flow has been estimated with reasonable accuracy. It can
be seen that the axial velocity is fairly constant across the test flow (Figure 17).
The variation in Pitot pressure seen in Figure 15 is due to the variation in
density across the test flow. The profile of radial velocity shows that the flow
angularity increases linearly with radius. This may pose a problem for
researchers who wish to test models with large widths.

Figure 18 shows the variation of rarefaction parameters, axial velocity and
density in the test flow ($t = 370\,\mu$s and $x = 225\,$mm) along the centerline of the
dump tank. From the axial profile of the breakdown parameter based on an
object size of 10 mm, it can be seen that at the nominal test location $P_D \approx 0.1$,
so we could expect strong non-continuum effects in the flow over a model of
this size. The large axial gradient of density is problematic for testing models
with large axial lengths (Figure 18). Overall, the computational data presented
in Figures 17 and 18 indicated that the test flow produced during low-density
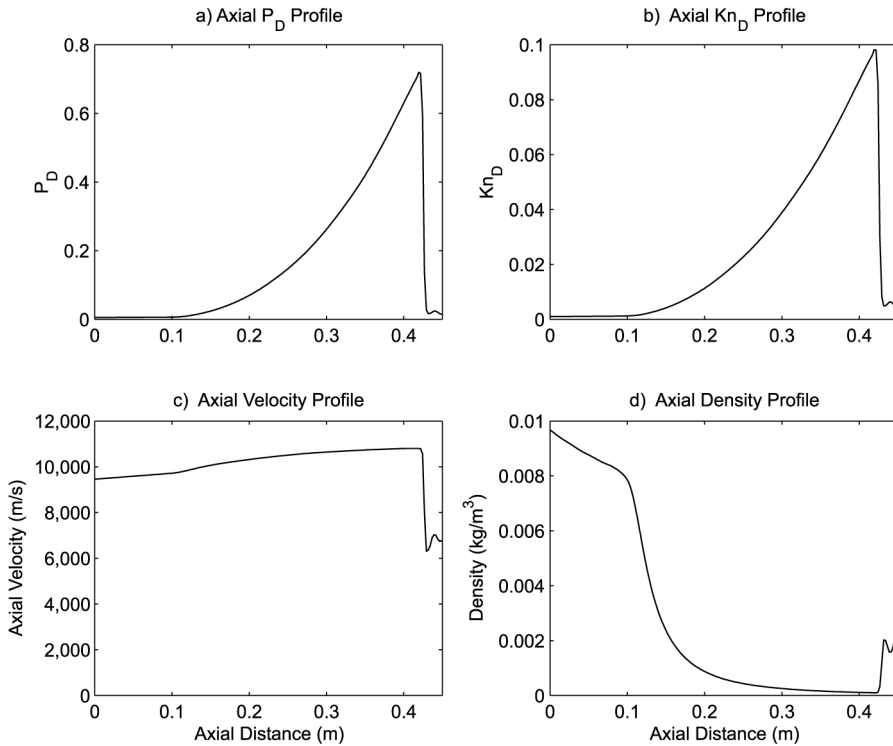
Figure 18.
Computed profiles of breakdown parameter, P_D, Knudsen number, Kn_D (based on $D = 10$ mm), axial velocity and density along the centerline in the dump tank. Profiles are from $t = 370\,\mu s$ when the secondary contact surface is located at $x \approx 425$ mm

operation of X1 is suitable for the testing of relatively compact models with small diameters and that the flow conditions are similar to those encountered during an aerobraking maneuver. This similarity will allow computational techniques such as DSMC to be experimentally calibrated at high-enthalpy flow conditions.

Conclusions

By using an expansion tube and further expanding the test gas as a free jet, rarefied flows at superorbital speeds can be produced in a laboratory facility. The flows produced in the X1 facility have been surveyed using bar-gauge pressure transducers and further details have been obtained via numerical simulation. There is good agreement between most of the experimental data and the simulation results; however, some of the simulation results, such as shock speed, should be better estimated using a non-equilibrium thermochemical model. The test section flows, as produced for this study, were reasonably uniform and could be used to test small aerodynamic models. Data from these tests could then be used to calibrate other CFD codes for high enthalpy rarefied flow.

References

Allegre, J. (1992), "The SR3 low density wind-tunnel: facility capabilities and research development", AIAA Paper 92-3972.

Bird, G.A. (1994), *Rarefied Gas Dynamics and the Direct Simulation of Gas Flows*, Claredon Press, Oxford.

Borque, B. (1999) "Development of hypervelocity wind tunnel for rarefied flow", Undergraduate Thesis, University of Queensland.

Cheng, H.K. and Emanuel, G. (1995), "Perspective on hypersonic nonequilibrium flow", *AIAA Journal*, Vol. 33 No. 3, pp. 385-400.

Chiu, H.H. (2000), "Development of a test facility for hypervelocity rarefied flows", Departmental Report 2000/09, Department of Mechanical Engineering, University of Queensland.

Dankert, C. (1996), "DLR Göttingen hypersonic vacuum wind tunnels V1G and V2G and high vacuum wind tunnel V3G", Brochure, DLR, SM-SK-ATD, Bunsenstrasse 10, D-37073 Göttingen, Germany.

Gupta, R.N. (1996), "Viscous shock-layer study of thermochemical nonequilibrium", *Journal of Thermophysics and Heat Transfer*, Vol. 10 No. 2, pp. 257-66.

Gupta, R.N., Moss, J.N. and Price, J.M. (1997), "Assessment of thermochemical nonequilibrium and slip effects for orbital re-entry experiment", *Journal of Thermophysics and Heat Transfer*, Vol. 11 No. 4, pp. 562-9.

Jacobs, P.A. (1998), "MB-CNS: a computer program for the simulation of transient compressible flows", 1998 Update, Department of Mechanical Engineering Report 7/98, The University of Queensland, Brisbane, available at: http://www.mech.uq.edu.au/staff/jacobs/cfd/mb_cns/doc/mb_cns.html

Jacobs, P.A. (1999), "L1d: a computer code for the quasi-one-dimensional modelling of transient-flow facilities", Technical Report 1/99, Department of Mechanical Engineering, The University of Queensland.

Jones, J.J. (1965), "Some performance characteristics of the LRC 33/4-inch pilot tube using and unheated hydrogen driver", *4th Hypervelocity Techniques Symposium*.

Macrossan, M.N. (1989), "The equilibrium flux method for the calculation of flows with non-equilibrium chemical reactions", *Journal of Computational Physics*, Vol. 80 No. 1, pp. 204-31.

Macrossan, M.M., Chiu, H.H. and Mee, D.J. (2000), "A test facility for hypervelocity rarefied flow", in Gallis, B. (Ed.), *Proceedings of the 22nd International Symposium on Rarefied Gas Dynamics*, American Institute of Physics, New York, NY, p. 772.

Morgan, R.G. (1997), "A review of the use of expansion tubes for creating superorbital flows", AIAA Paper 97-0279.

Morgan, R.G. and Stalker, R.J. (1992), "Double diaphragm driven free piston expansion tube", *Proceedings of the 18th International Symposium on Shock Tubes and Waves*.

Moss, J.N. (1995), "Rarefied hypersonic flows: simulation, experiments and applications", *Proceedings of the 19th International Symposium on Rarefied Gas Dynamics*.

Neely, A.J. (1995) "Experimental and analytical study of a pilot superorbital expansion tube for aerothermodynamic testing to 13 km/s in air", PhD thesis, University of Queensland.

Neely, A.J. and Morgan, R.G. (1994), "The superorbital expansion tube concept, experiment and analysis", *The Aeronautical Journal*, Vol. 98 No. 973, pp. 97-105.

Paull, A., Stalker, R.J. and Stringer, I.A. (1988), "Experiments on an expansion tube with a free piston driver", *AIAA 15th Aero. Testing Conference*.

Petrie-Repar, P.J. and Jacobs, P.A. (1998), "A computational study of shock speeds in high performance shock tubes", *Shock Waves*, Vol. 8 No. 2, pp. 79-91.

Roberts, G.T., Kendall, M.A. and Morgan, R.G. (1997), "Shock-diaphragm interaction in expansion tubes", *21st International Symposium on Shock Waves*.

Shinn, J.L. and Miller, C.G. (1978), "Experimental perfect-gas study of expansion-tube flow characteristics", NASA Technical Paper 1317.

Smith, A.L. and Mee, D.J. (1996), "Dynamic strain measurement using piezoelectric polymer film", *Journal of Strain Analysis*, Vol. 31 No. 6, pp. 463-5.

Trimpi, R.L. (1962), "A preliminary theoretical study of the expansion tube, a new device for producing high-enthalpy short-duration hypersonic gas flows", NASA Technical Report R-133.

Wada, Y. and Liou, M.S. (1994), "A flux splitting scheme with high-resolution and robustness for discontinuities", AIAA Paper 94-0083.

Wendt, M., Macrossan, M., Jacobs, P.A. and Mee, D.J. (1998), "Pilot study for a rarefied hypervelocity test facility", *13th Australasian Fluid Mechanics, Conference*.

Wheatley, V. (2000) "Modelling low-density flow in hypersonic impulse facilities", Masters of Engineering Science Thesis, The University of Queensland.

Wilson, G.J. (1992), "Time dependent quasi-one dimensional simulations of high enthalpy pulse facilities", *AIAA 4th International Aerospace Planes Conference*.